1-1-2017

Voltammetric Enhancement of Li-Ion Conduction in Al-Doped Li7-xLa3Zr2O12 Solid Electrolyte

Yu-Ting Chen
National Taiwan University

Anirudha Jena
National Taiwan University, National Taipei University of Technology

Wei Kong Pang
University of Wollongong, Australian Nuclear Science and Technology Organization, wkpang@uow.edu.au

Vanessa K. Peterson
University of Wollongong, Australian Nuclear Science and Technology Organization

Hwo-Shuenn Sheu
National Synchrotron Radiation Research Center Taiwan

See next page for additional authors

Recommended Citation

Voltammetric Enhancement of Li-Ion Conduction in Al-Doped Li7-xLa3Zr2O12 Solid Electrolyte

Abstract

2017 American Chemical Society. Al-doped $Li_{7-x}La_3Zr_2O_{12}$ is found to be more ionically conductive following voltammetric treatment in an all-solid-state $Li|Li_{7-x}La_3Zr_2O_{12}|Li$ cell configuration. This result is consistent with electrical impedance spectroscopy measurements, which reveal that the activation energy for lithium diffusion is reduced from 0.32 to 0.26 eV following voltammetric treatment. The Li deposition-dissolution signal has been observed in the voltammograms, and neutron powder diffraction shows an increase in the lithium content of the $Li_{7-x}La_3Zr_2O_{12}$. Furthermore, X-ray photoelectron spectroscopy indicates a local rearrangement of O, resulting in a reduction of defects following voltammetric treatment, with the enhanced conductivity attributable to both the reduction of defect oxygen and increased lithium content. This work, therefore, reveals such voltammetric treatment as a simple and inexpensive alternative to existing doping approaches to boost the electrochemical performance of $Li_{7-x}La_3Zr_2O_{12}$. The findings can improve the future development of all-solid-state Li-ion batteries. On the other hand, our approach to understanding the conductivity enhancement via voltammetric treatment may provide a better alteration in the ionic conduction of solid electrolytes during solid-state battery operation. (Graph Presented).

Disciplines

Engineering | Physical Sciences and Mathematics

Publication Details

Authors

Yu-Ting Chen, Anirudha Jena, Wei Kong Pang, Vanessa K. Peterson, Hwo-Shuenn Sheu, Ho Chang, and Ru-Shi Liu

Voltammetric Enhancement of Li-Ion Conduction in Al-doped $Li_{7-x}La_3Zr_2O_{12}$ Solid Electrolyte

Yu-Ting Chen, [†] *Anirudha Jena,* [†,‡] *Wei Kong Pang,* [⊥,‖] *Vanessa K. Peterson,* [⊥,‖] *Hwo-Shuenn Sheu,* [Δ] *Ho Chang,* [*,‡] *Ru-Shi Liu* [*,†,‡]

[†] Department of Chemistry, National Taiwan University, Taipei 10617, Taiwan

[‡] Department of Mechanical Engineering and Graduate Institute of Manufacturing Technology, National Taipei University of Technology, Taipei 10608, Taiwan

[⊥] Australian Centre for Neutron Scattering, Australian Nuclear Science and Technology Organization, NSW 2232, Australia

[‖] Institute for Superconducting and Electronic Materials, University of Wollongong, Squires Way, North Wollongong, NSW 2500, Australia

[Δ] National Synchrotron Radiation Research Center, Hsinchu 30076, Taiwan

ABSTRACT: Al-doped $Li_{7-x}La_3Zr_2O_{12}$ is found to be more ionically conductive following voltammetric treatment in an all-solid-state $Li \mid Li_{7-x}La_3Zr_2O_{12} \mid Li$ cell configuration. This result is consistent with electrical impedance spectroscopy measurements, which reveal that the activation energy for lithium diffusion is reduced from 0.32 eV to 0.26 eV following voltammetric treatment. The Li deposition–dissolution signal has been observed in the voltammograms, and neutron powder diffraction shows an increase in the lithium content of the $Li_{7-x}La_3Zr_2O_{12}$. Furthermore, X-ray photoelectron spectroscopy indicates a local rearrangement of O, resulting in a reduction of defects following voltammetric treatment, with the enhanced conductivity attributable to both the reduction of defect oxygen and increased lithium content. This work, therefore, reveals such voltammetric treatment as a simple and inexpensive alternative to existing doping approaches to boost the electrochemical performance of $Li_{7-x}La_3Zr_2O_{12}$. The findings can improve the future development of all-solid-state Li-ion batteries. On the other hand, our approach to understanding the conductivity enhancement via voltammetric treatment may provide a better alteration in the ionic conduction of solid electrolytes during solid-state battery operation.

1. Introduction

Cutting edge Li-ion battery (LIB) technology currently utilizes liquid or organic-based electrolytes; however, LIB miniaturization, as required by small-scale electronics, is a challenge because of safety issues. Solid-state Li-ion conductors are promising alternatives to conventional LIB electrolytes, mitigating the safety issues of dendritic Li growth in organic-based LIB electrolytes.[1-2] Among Li-ion conducting materials, $Li_7La_3Zr_2O_{12}$ (LLZO), possessing a garnet-type crystal structure, is of particular interest for application as a solid LIB electrolyte because of its suitable ionic conductivity, chemical stability in a wide potential range, and ease of scaling for industrial applications.[3] Murugan et al. first highlighted LLZO as a new garnet-type solid-state electrolyte, showing that the material featured a high stability, with Li-ion conductivities reaching 2.5×10^{-4} S/cm.[4] LLZO can crystallize in cubic or tetragonal symmetry phases depending on the synthesis conditions. Cubic LLZO possesses $Ia\overline{3}d$ space group symmetry with La, Zr, and O atoms located at 24c, 16a, and 96h sites, respectively, whereas Li occupies both 24d tetrahedral and 96h octahedral sites.[5] Tetragonal LLZO possesses $I4_1/acd$ space group symmetry with La, Zr, and O atoms located at 8b (and 16e), 16c, and 32g, respectively. Importantly, the conductivity of tetragonal LLZO is two orders lower than for cubic LLZO,[6] and doping with Al, which preferably occupies 24d site,[7] is an effective method to stabilize the more favorable cubic LLZO phase.[8-9] Nevertheless, the conductivity of LLZO needs to be enhanced further to satisfy industrial application criteria. Beyond the stabilization of the favorable crystal form, elemental doping has also been shown to enhance the ionic conductivity of LLZO from 10^{-4} to 10^{-3} S/cm by including elements such as Ta [10] and Ga [11]. Improvement of ionic conductivity by sintering under oxygen has been reported by Guo et al.[12] However, due to low abundance and expensive, industrial production still remains a challenge. Moreover, interfacial

stability issues arising between the Li-ion conductor and electrode materials within a battery remain unresolved. Although solid-state batteries are currently emerging as future energy storage devices, understanding the change in the Li-ion conduction during the battery operation has yet to be addressed.

The mechanism of Li-ion conduction in LLZO has been studied by many researchers, who have focused on the bottlenecks to improving Li-ion conduction. Xu et al.[13] and Miara et al.[14] calculated the activation energy for the Li-ion jump-type diffusion to be 0.26 and 0.24 eV, respectively. These values are somewhat lower than the experimentally measured activation energy for Li-ion diffusion in the Al-doped LLZO (without other doping elements) of 0.3 eV. [8, 15-17]

Galvanostatic method has been employed to simulate the working condition of LLZO in batteries and an abrupt voltage (resistance) drop was observed when larger current density was applied. The phenomenon was ascribed exclusively to Li dendrite formation.[18-21] However, a step-function current was applied in the above research, which is not ideal for observing the intermediate state of LLZO during the voltage drop.

The existing researches only proposed solutions to alleviate such phenomenon. Rather than suppressing, the present work aims to take advantage of such phenomenon and probe the intermediate state of LLZO during the resistance drop. We thus propose a voltammetric treatment to study the electrochemical behavior of Al-doped LLZO. Instead of non-continuous current, we applied a smoothly-evolved potential to LLZO. After the treatment, the ionic conductivity of LLZO is largely enhanced without significantly raising the electronic conductivity. Subsequent characterizations are conducted to figure out the mechanism of such

increment in ionic conduction without affecting the electronic migration. Both Li (non-blocking) and Au (blocking) electrodes systems are utilized in the electrochemical analyses. Neutron powder diffraction (NPD) method is used to determine the change in ionic concentration of the Al-doped LLZO before and after voltammetric cycles. X-ray photoelectron spectroscopy (XPS) is used to identify the realignment of the oxygen skeleton as essential in the mechanism of conductivity enhancement. We observe there is a rearrangement of ions occurs during the electrochemical measurements; this observation has never been addressed before.

2. Experimental Methods

2.1. Syntheses of the material

Al-doped LLZO was synthesized through the solid-state reaction of LiOH (+10% excess, Alfa Aesar 98% purity, pre-heated at 200 ℃ for 6h), La_2O_3 (Sigma-Aldrich, 99.9% purity, pre-heated at 900 ℃ for 12h)[3], ZrO_2 (Alfa Aesar 99.7% purity), and Al_2O_3 (1 wt.% of LLZO, Sigma 99.95% purity) in stoichiometric quantities following ball-milling in isopropanol using PM-100 zirconia balls at 300 rpm for 6 h. The acquired slurry was dried at 90 ℃, and the well-mixed powder was pre-heated to 900 ℃ for 4 h and then calcined at 1230 ℃ for 12 h to obtain LLZO. The LLZO was ground by hand into powder with #200 mesh and then uni-axially pressed into 12-mm-diameter pellets at 1734 MPa. The pellets were subsequently isolated with a thick layer of mother powder to mitigate Li evaporation and avoid Al inclusion from corundum crucibles and sintered in a multistep method to acquire the pure LLZO phase.[22] This process involved heating to 1100 ℃ at 5 ℃/min and holding for 4 h and heating to 1230 ℃ at 5 ℃/min and holding for 12 h before cooling to room temperature. All heating processes were conducted under atmospheric condition using covered corundum crucibles. After sintering, the pellets were

polished to 1200 mesh. The density of the pellets was 92% relative to the theoretical crystal density. All pellets were stored in an argon glove box to prevent carbon dioxide and moisture contamination, which can affect the electrochemical properties. [23]

2.2. Electrochemical analysis

All the LLZO pellets used in electrochemical testing were 4.5–5.5 mm thick unless otherwise specified. Both sides of the pellets were repeatedly polished to get mirror-polished surface and then assembled in a Swagelok cell using Au | LLZO | Au and Li | LLZO | Li configuration for further study. In the Au electrode system, both sides of the LLZO were sputtered with Au and connected by wire to the instrument. In the Li electrode system, the cell was assembled in the argon-filled glove box. LLZO pellets were pressed with Li foil on both sides and sealed in Swagelok cells. Unless otherwise specified, all the electrochemical experiments were conducted 24 h after cell assembly to ensure that the contact between Li foil and LLZO was stable. The voltammetric treatment was applied to LLZO using Li | LLZO | Li configuration with potential scanning from 0 to -5 V, then to 5 V, and back to 0 V at a scan rate of 0.5 mV/s in each cycle (5 cycles were done) with CHI611E instrument. Following the treatment, the Li foils were changed, and LLZO pellets were re-polished between different instrumental measurements. For each characterization set, LLZO pellets before (denoted LLZO_NV) and after (LLZO_V) voltammetric treatment were obtained from the same sintering batch. The Li-ion conductivity of LLZO was obtained using AC impedance spectroscopy with a signal amplitude of 0.1 V from 3 MHz to 1 Hz and a Zahner Elektrik IM6eX potentiostat-frequency analyzer. Impedance data with both Li and Au electrode systems were acquired. This system with Au electrodes was utilized to study the relationship between temperature and conductivity from 30 to 170 ℃. All impedance data were analyzed with the Zview software and fitted with the R(R-CPE)(R-CPE)

model. The electronic conductivity of LLZO was acquired with DC polarization method using CHI611E instrument. The data were collected using polarization potential of 0.1 V and holding time of 20000 seconds.

2.3. Coin cell assembly

A positive electrode slurry comprising $LiNi_{0.5}Co_{0.2}Mn_{0.3}O_2$ (NCM532), SuperP carbon black, KS6 carbon black, and polyvinylidene fluoride (PVDF) in the weight ratio 7.5:0.5:1:1, respectively, was made using a suitable amount of N-methyl-2-pyrrolidon (NMP). The slurry was well-mixed and coated on Al foil, dried, and cut into a round shape. The positive electrode was assembled into 2032 type coin cell with Li anode and electrolyte with ethylene carbonate/dimethyl carbonate (1:1) in an argon-filled glove box.

2.4. Solid-state cell assembly

A positive electrode slurry composed of NCM532, SuperP carbon black, KS6 carbon black, polyvinylidene fluoride (PVDF) and LiTFSI (bis-trifluoromethane sulfonamide) lithium salt in the weight ratio 7.5:0.5:1:1:5.5, respectively, was made using a suitable amount of NMP. It is worth mentioned that mixing LiTFSI and PVDF can form a decent polymer electrolyte.[24] The slurry was well-mixed and coated on one side of a 3-mm LLZO pellet, while the other side was coated with a slurry comprising LiTFSI and PVDF in a weight ratio 1:1 to enhance the lithium-ion transfer at the interface between the LLZO and Li foil-negative electrode. The pellet was dried in a vacuum oven for 12 h and sealed in a Swagelok cell in an argon glovebox. The cell was tested at 80 ℃ between 2.8 and 4.15 V. Each discharge was performed using a potential hold at 2.8 V until the current decreased to 0.01 C.

X-ray diffraction (XRD) was employed to test the phase purity of the synthesized LLZO. LLZO pellets were crushed into a powder and sealed into a capillary, where data were obtained using the 01C2 beamline of the National Synchrotron Radiation Research Center (NSRRC) in Taiwan. An X-ray wavelength of 0.77446(1) Å was used, as determined using the LaB_6 (SRM660c), and data were recorded between 5 and 44.9° 2θ. NPD was used to obtain the Li-ion concentration in the sample where the neutron scattering cross-section is not dependent on the atomic number and where good elemental contrast could be obtained. Data for the 8-mm diameter LLZO pellets were obtained using the high-resolution neutron powder diffractometer, ECHIDNA, at the Australian Nuclear Science and Technology Organization (ANSTO); with a neutron wavelength of 1.62362(4) Å determined using the LaB_6 (SRM660b) between 13 and 163.9° 2θ.[25] GSAS II was employed to refine the structural model obtained from the ICSD 422259 file.[26] The refined parameters of NPD include the background coefficient; zero shift; peak shape parameter; positional parameter of O and Li at the 96*h* site; the site occupancy factor of Zr at the 16*a* site, O at the 96*h* site, Li at the 24*d* site, and Li at the 96*h* site; and the isotropic atomic displacement parameters of La at the 24*c* site, Zr at the 16*a* site, and O at the 96*h* site. The occupancy of Al at 24*d* site was fixed at 0.06, which is close to the theoretical value derived from 1 wt.% addition of Al_2O_3.[7] The occupancy of La is set to be unity and the values of other atoms are the occupancies relative to La. Li was not refined in XRD data, owing to its low sensitivity and was fixed as the value obtained in NPD refinement. The refinement conditions of all the other parameters were the same as those obtained through NPD.

Core-level XPS of LLZO was performed using Al Kα radiation (20 mA, 1486.7 eV) with a PHI Quantera SXM. LLZO pellets were polished to remove surface impurities, and the solid electrolyte interphase (SEI) [27] beforehand and loaded immediately into the instrument. The

surface was etched with an argon beam for 10 min to remove surface contamination and Li_2CO_3. Zr 3d, La 3d, and O 1s spectra were collected. The acquired data were processed with the CasaXPS software. A Voigt-type line shape and Shirley-type background were applied. Constraints applied in the Zr 3d deconvolution were that the area ratio of $3d_{3/2}$ and $3d_{5/2}$ peak pairs was 2:3 (following the degeneracy of the spin-orbit coupling). The following constraints were applied in the La 3d deconvolution.[28] The area ratio of $3d_{3/2}$ and $3d_{5/2}$ peak pairs was set to 2:3, and peak pairs were deconvoluted into main peaks, satellites (bonding and anti-bonding of ligand charge transfer), and plasmons. The full width at half maximum and energy separation (16.8 eV) were identical for each spin-orbit coupling peak pair. The bonding and anti-bonding components of the satellites were fixed to be the same area. No constraint was applied in the O 1s deconvolution. The X-ray absorption near edge spectra for LLZO was collected for powders sprayed uniformly onto tape at the 01C1 (for the Zr K-edge) and 17C (for the La L_3 edge) beamlines at the NSRRC.

3. Results and discussion

Fig. 1 shows the cubic LLZO refinement profile using XRD, indicating a highly crystalline phase-pure material. The refined crystallographic parameters are given in supplementary information (SI) **Table 1**. The occupancy ratio of La and Zr is close to unity. The lithium occupancy will be referred to the NPD results for their accurate determination.
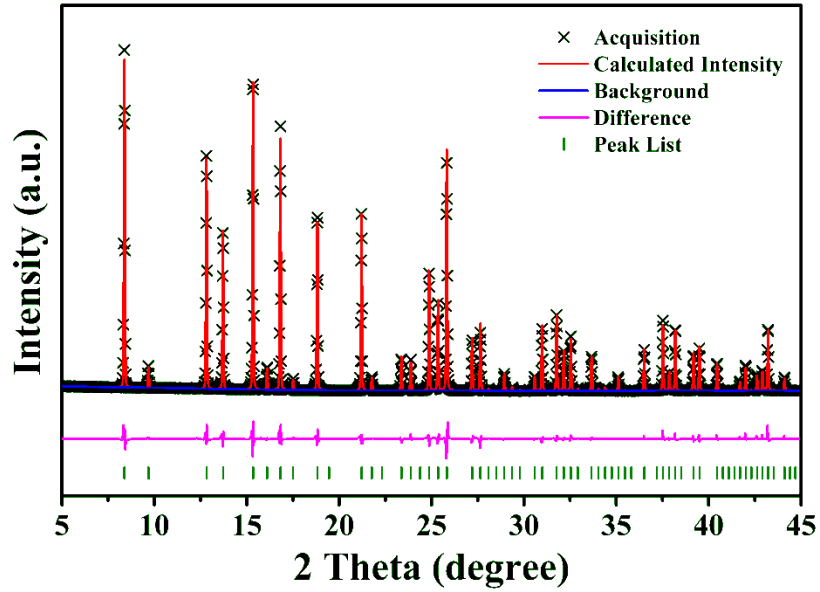
Fig. 1. Rietveld refinement profiles for LLZO using XRD data

In the voltammetric treatment, the I-V profile of five scanning cycles was recorded for the Li | LLZO | Li cell, as shown in **Fig. 2**. Since the system is symmetric, the OCV was ~0 V and reverse potential scans were also performed. Following the first cycle of activation process, the Li deposition–dissolution peak appeared and persisted in both polarization directions for the remaining cycles, with peak height i_p (current maximum in ampere) increasing with cycle number. The Li deposition–dissolution peak height reflects the activation state of LLZO. By applying the Randles–Sevcik equation (1) [29], the diffusion coefficient, D (cm^2/s), of lithium can be obtained,

$$i_p = 0.4463nFAC \left(\frac{nFvD}{RT}\right)^{1/2} \qquad (1)$$

where n is the number of electrons transferred in the redox event, A is the electrode area in cm^2, F is the Faraday current, C is the concentration in mol/cm^3, v is the scan rate in V/s, R is the gas constant, and T is the temperature in K.
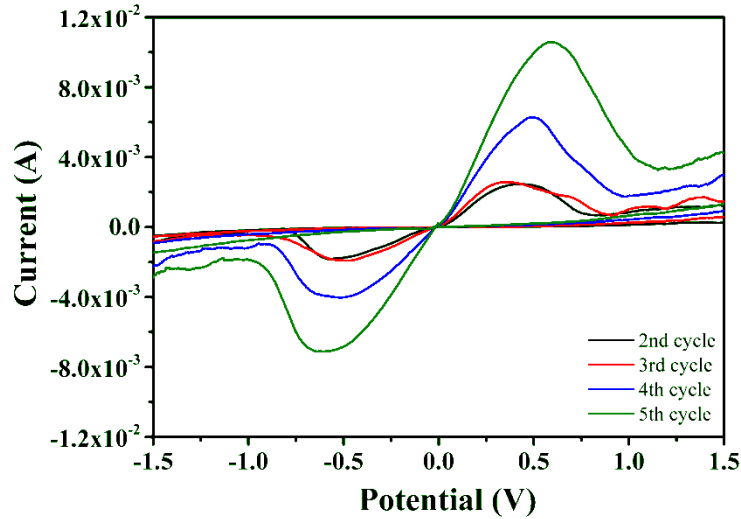
**Fig. 2**. The I-V profiles of cyclic voltammetry with Li | LLZO | Li cell.

The results indicate an increasing diffusion of Li ions. The peak heights in the reverse polarization direction are lower; this phenomenon may arise from differences in the effective contact areas. After voltammogram cycles, the LLZO surface show blackening which propagates thoroughly through the bulk (**Fig. S1**). ZrO$_2$ was also observed to undergo electrochemical blackening after polarization, which may result from injection of charge into oxygen vacancies or reduction of cations.[30-31]

The results of AC impedance measurements with Li | LLZO | Li cells and Au | LLZO | Au cells are presented in **Fig. 3**. In both systems, the semicircle with the highest frequency (of order MHz) can be assigned to the total conductivity, including the bulk and grain boundary components, of LLZO.[8, 11, 32] A complete low-frequency semicircle (of order kHz) resulting from

11

charge transfer of Li ions on the interface between LLZO and Li metal exists in Li | LLZO | Li cells and this presents the reversible nature in such system. In Au | LLZO | Au cells, the low-frequency semicircle is substituted with a tail that can be assigned to capacitor behavior of blocking system.[11, 32] The results of Li | LLZO | Li cells are presented in **Figs. 3**(a) and (b). The total ionic conductivity of LLZO_NV is 3.4×10^{-4} S/cm and increased to 1.2×10^{-3} S/cm following cycling (LLZO_V); this value was almost three times that of LLZO_NV. Total ionic conductivities of LLZO_NV and LLZO_V acquired with Au | LLZO | Au cells were 4.0×10^{-4} S/cm and 4.6×10^{-3} S/cm, which are analogous to Li | LLZO | Li cells and present similar ionic conductivity values of LLZO_NV and conductivity enhancement after voltammetric treatment. The corresponding Arrhenius plots for LLZO_NV and LLZO_V are shown in **Fig. 3**(c), where the activation energy (E_a) in eV was determined using equation 2.[33]

$$\sigma = \frac{\sigma_0}{T} e^{\frac{-E_a}{KT}} \qquad\qquad (2)$$

where σ is conductivity, T is the temperature in K, and K is the Boltzmann constant. The E_a for Li-ion conduction in LLZO_NV and LLZO_V were 0.32 eV and 0.26 eV, respectively, indicating an easier Li-ion transport mechanism for LLZO after the voltammetric treatment, with this E_a in good agreement with reported simulation values.[13-14]
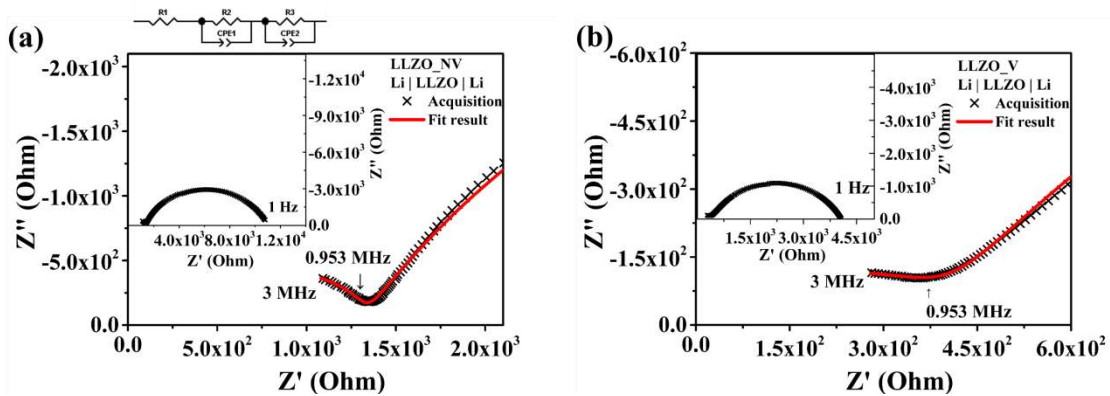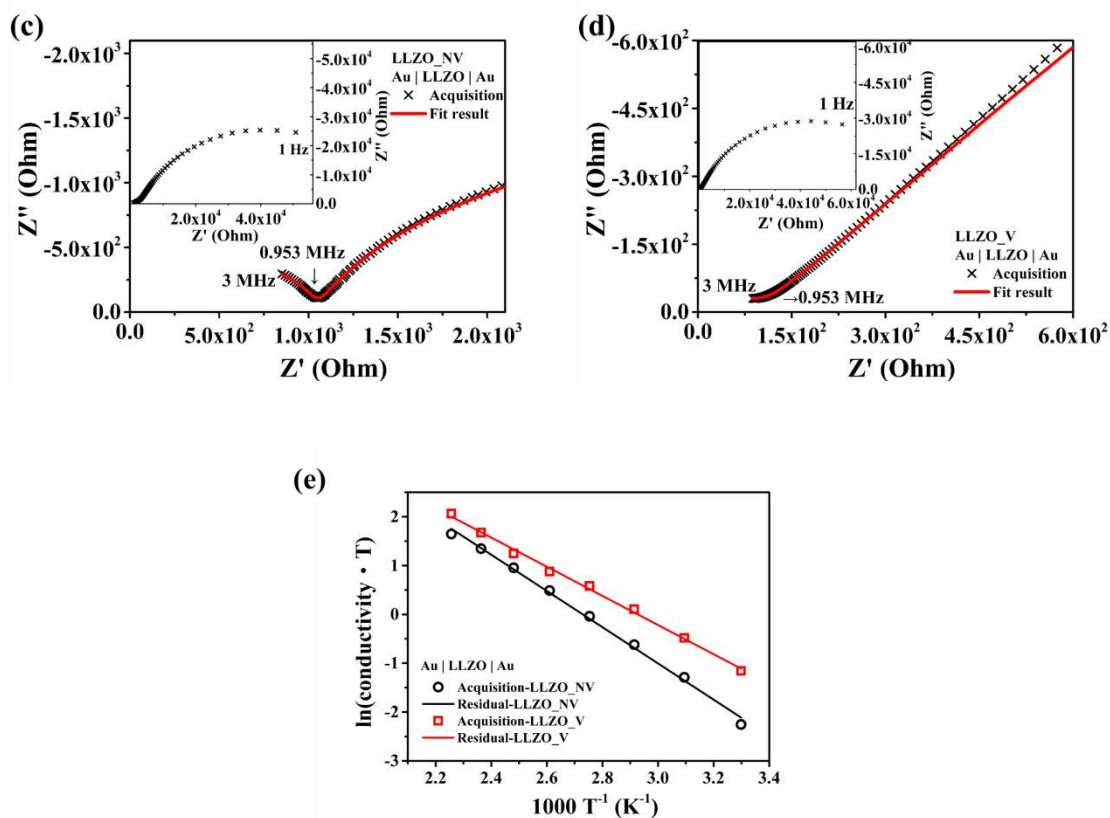
Fig. 3. EIS data and fitting results for LLZO samples in (a), (b) Li | LLZO | Li and (c), (d) Au | LLZO | Au cells. (a), (c) LLZO_NV; (b), (d) LLZO_V; (e) Arrhenius plots of LLZO_NV and LLZO_V.

Fig. 4 shows Rietveld refinement profiles for the LLZO_NV and LLZO_V using NPD data with the crystallographic and refinement results listed in SI **Table 2**. Before voltammetric treatment, the LLZO had fully occupied La, Zr, and O and ~4.98 Li atoms per formula unit. After voltammetric treatment, the total Li content increased to ~5.55 Li atoms per formula unit, probably a result of the inclusion of Li ions through the oxidation reaction of Li metal during voltammetric treatment.
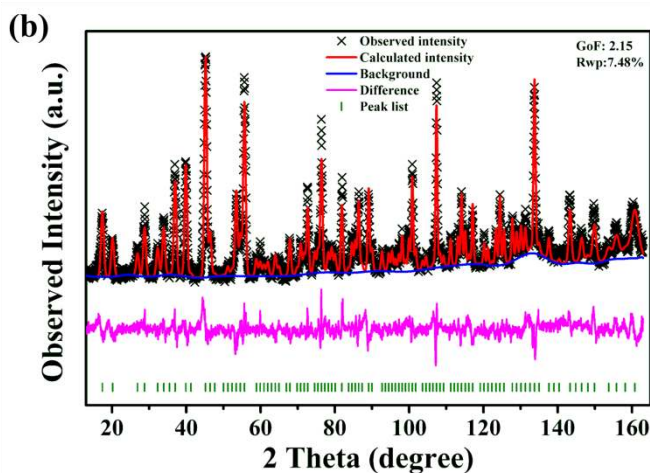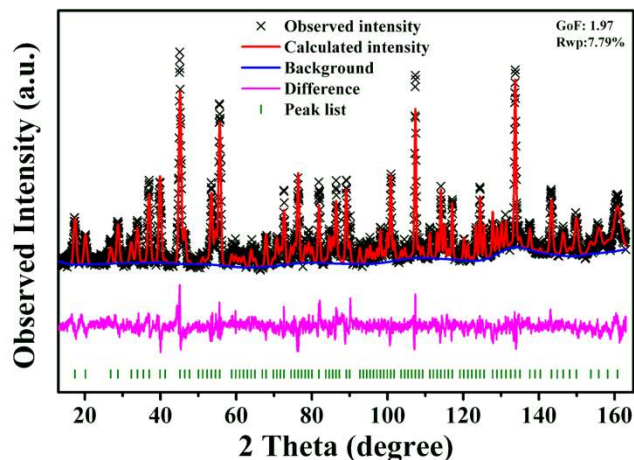
Fig. 4. Rietveld refinement profiles for LLZO using neutron powder diffraction data (a) before voltammetric treatment and (b) after voltammetric treatment.

Fig. 5 shows the XPS of Zr 3d, La 3d, and O 1s for LLZO_NV and LLZO_V samples with the deconvoluted peak positions presented in SI **Table 3**. The spin-orbit splitting of Zr 3d found to be 2.4 eV for both samples; this value is consistent with earlier reports.[34-35] The binding energies of Zr 3d are found to be 180.8 and 181.4 eV for LLZO_NV and LLZO_V, respectively. These values lie between the values of Zr^{4+} and Zr^+ in zirconium oxide. The La $3d_{5/2}$ main peaks

for LLZO_NV and LLZO_V are located at 833.2 and 833.7 eV, respectively, and are lower than those for La in La_2O_3 and $La(OH)_3$ (La_2O_3 = 834.9 eV and $La(OH)_3$ = 835.1 eV [28]). Both Zr and La spectra reveal a binding energy that is lower for the corresponding oxides with the same formal charge.
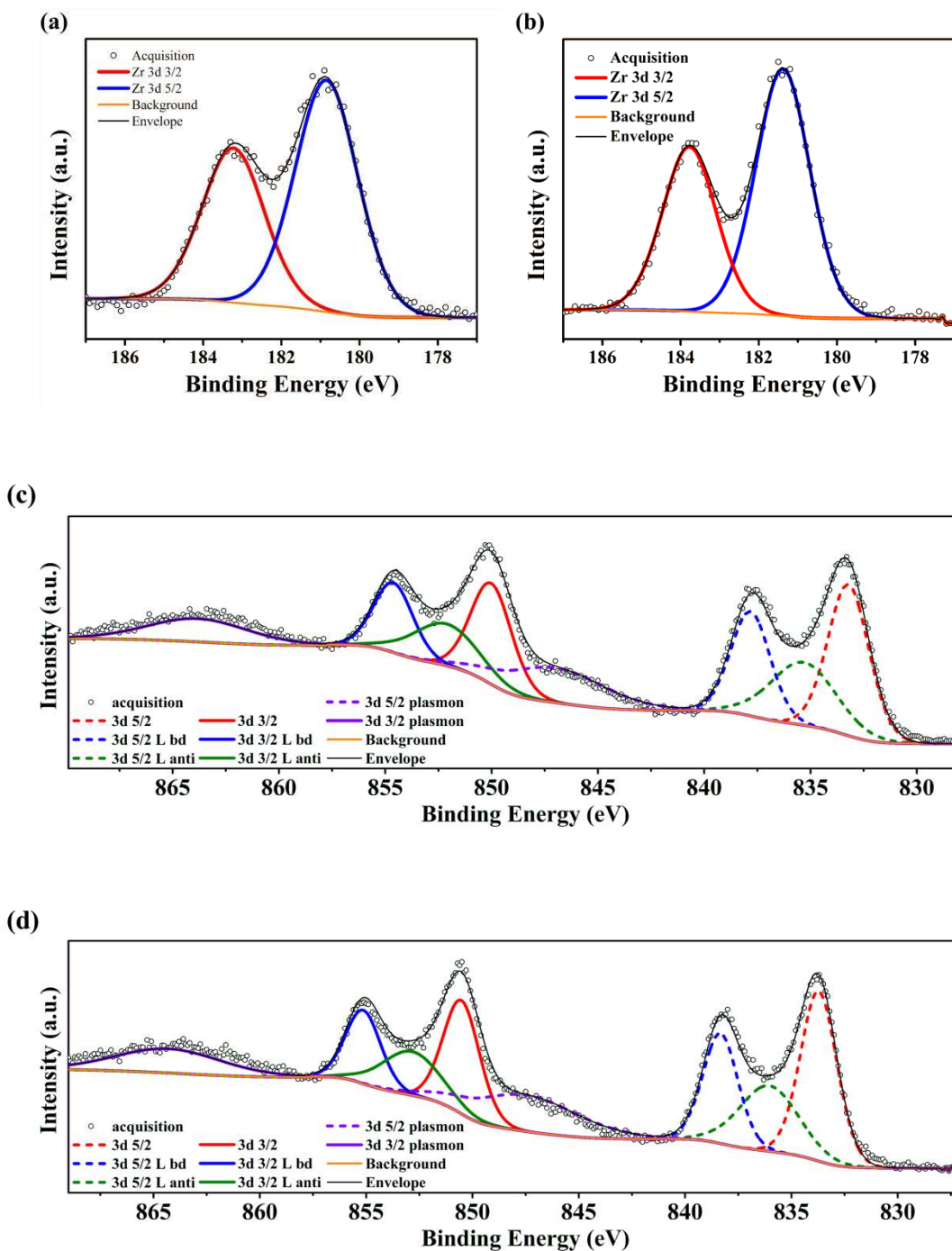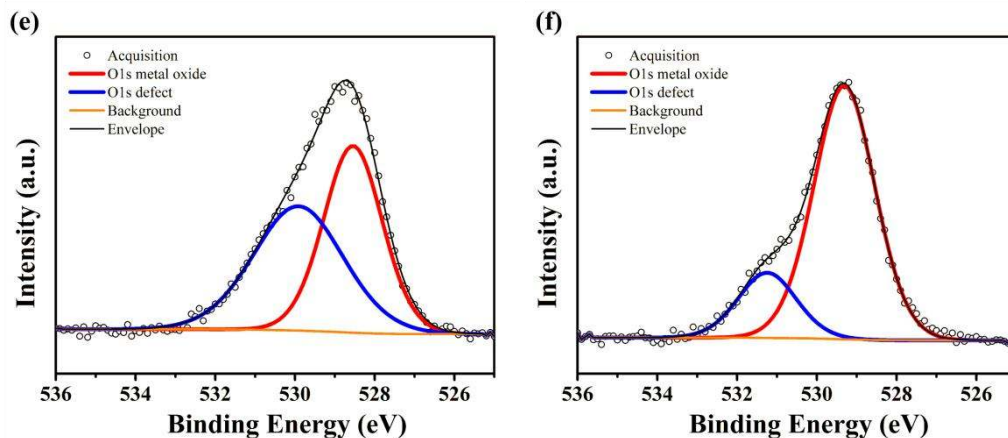
Fig. 5. XPS data and deconvoluted Zr 3d spectra for (a) LLZO_NV and (b) LLZO_V, La 3d spectra for (c) LLZO_NV and (d) LLZO_V, and O 1s spectra for (e) LLZO_NV and (f) LLZO_V

The phenomenon was also presented in X-ray absorption near-edge spectroscopy by showing lower absorption edge energies compared to corresponding oxide standard (**Fig. 6**). Nevertheless, the chemical environment of LLZO is different from that of the corresponding oxides as a result of the three different cations, complicating the determination of the chemical state using the pure oxide reference spectra. Importantly, an increased binding energy of both Zr and La following voltammetric treatment is found and may have arisen from the inclusion of additional Li ions. The O 1s XPS data of both samples can be deconvoluted into two peaks located at 528.5 and 529.9 eV for LLZO_NV. There is a shift of these peaks to 529.3 and 531.2 eV for the LLZO_V sample. The O 1s reference spectra for ZrO_2 show peaks at 531.0, 531.4, and 532.6 eV,[35] for La(OH)$_3$, the main peak at 531.3 eV, and for La_2O_3 at 530.3 eV,[28] with none of these describing well the spectrum for LLZO. In other bimetal oxide compounds and oxygen conductor electrolytes, the lower energy peak in the O 1s spectrum is commonly assigned as lattice oxygen in metal oxides while the other to surface, hydroxyl bonding, or defects,[10, 36-38] which are all

imperfectly arranged oxygen. Interestingly, while the total peak area for features in the O 1s spectra for LLZO_NV and LLZO_V are similar, the intensity of the peak assigned to lattice oxygen is much stronger for the LLZO_V than the LLZO_NV sample. This result indicates that defect oxygen in LLZO may rearrange into well-aligned lattice oxygen during the voltammetric treatment.
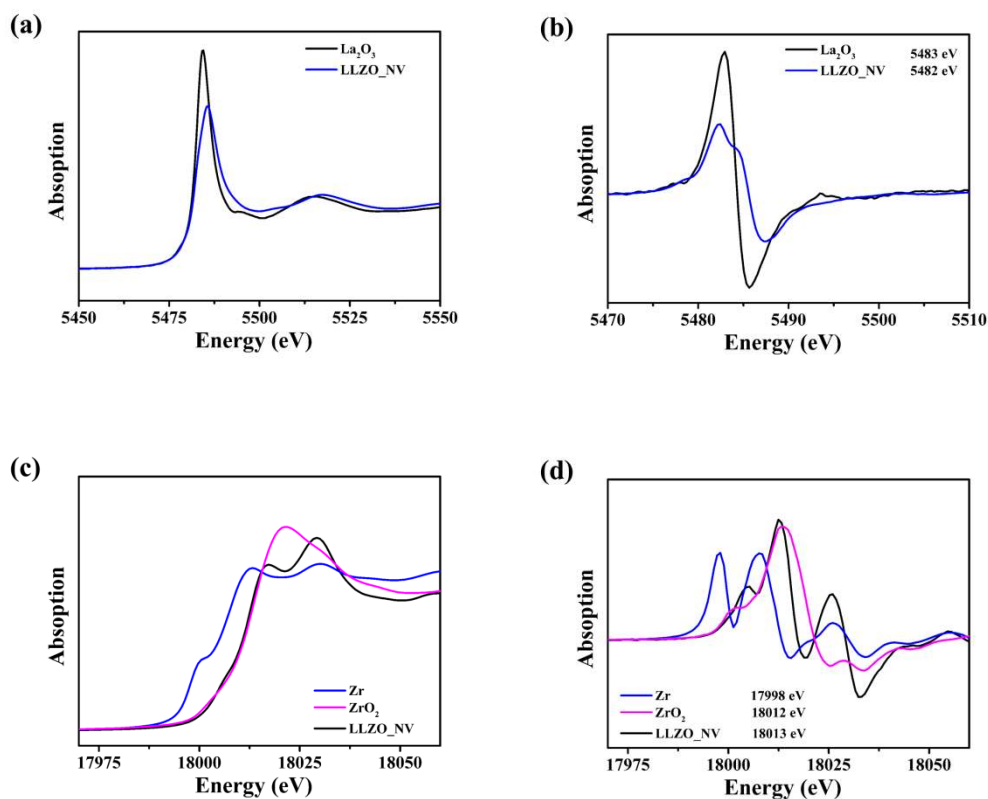
Fig. 6. XANES data at the (a) La L3 and (c) Zr K-edge and first derivative of data at the (b) La L3 and (d) Zr K-edge

The enhancement of conductivity in LLZO has been studied using physical and electrochemical analysis techniques. The increased conductivity has been discussed in light of both an increased Li content and the rearrangement of oxygen. The optimum Li concentration for $Li_{7-x}La_3Zr_{2-x}Ta_xO_{12}$ was found to be approximately 6.5 Li atoms per formula unit [39] and thus

increasing Li concentration when below 6.5 Li atoms per formula is beneficial to ionic conductivity.

Notably, both $La_2Zr_2O_7$ and ZrO_2 conduct oxygen,[30-31, 40] therefore, the mobility of oxygen atoms in LLZO is implied. Li mobility is also known to be influenced by the arrangement of the anionic framework,[41] where the local arrangement of oxygen below the limit of detection for average structural methods such as NPD may facilitate Li-ion migration. Such a mechanism is consistent with the lower activation energy for Li-ion diffusion in the LLZO following voltammetric treatment, as evident from the Arrhenius plots.

Since polarization with non-blocking electrodes may induce strong electron conduction,[18-21] electron conductivities of the LLZO samples must be measured. **Fig. 7** shows the DC polarization plots of LLZO_NV and LLZO_V. Upon polarizing, the currents both drop quickly and later gradually reach the asymptotes located at 2.7×10^{-8} A for LLZO_NV and 2.4×10^{-7} A for LLZO_V. The conductivity of LLZO did increase from 1.2×10^{-7} S/cm to 1.1×10^{-6} S/cm after voltammetric treatment. However, the ionic conductivity of LLZO_V is still over 10^3 times larger than electronic conductivity. Therefore, the ionic transference number as per the equation 3 [42] is still close to 1 after voltammetric treatment.

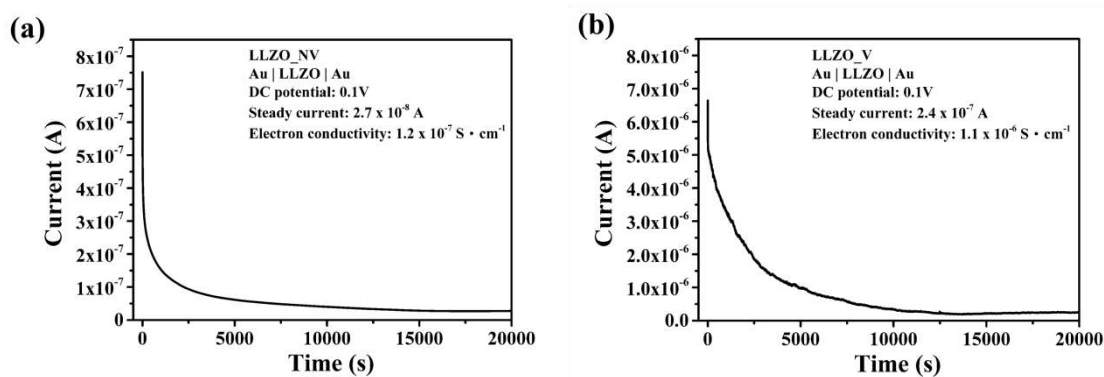$$t_{ion} = \frac{\sigma_{ion}}{\sigma_{e^-}+\sigma_{hole}} \qquad (3)$$

Fig. 7. DC polarization of (a) LLZO_NV and (b) LLZO_V samples.

Over-treating LLZO pellets will induce strong electronic conductivity and eventually lead to short circuit as reported previously.[18-21] **Fig. S2** (a) shows the color difference between pellets that experienced 5 and 8 voltammetric cycles. The color of 8-cycles sample is deeper than the other one. **Fig. S2** (b) is the I-V profile of 8th voltammetric cycle. The current increases quickly at -3 V and later saturates the instrument. This has been widely attributed to Li dendrite formation. Li^0 form and propagate through the voids present within the LLZO pellet.[43] Since oxygen drift was discovered through XPS, LLZO may also share the similar mechanism on electronic conductivity increment as in the oxygen conductor ZrO_2 through the formation of oxygen vacancies, oxygen evolution or Zr reduction. In the first 5 voltammetric cycles, the redox reaction of crystal framework did occur but the dendrites are less interconnected, hence induces slight electronic conductivity. In the following cycles, the dendrite network develops rapidly (results in deeper color) and the electronic conductivity eventually surpasses ionic conductivity. Nevertheless, as long as the cycle number is carefully chosen, the electrochemical property of LLZO can be optimized with the voltammetric treatment.

The viability of the LLZO_V sample for use as a solid-state battery is demonstrated in a half-cell, with **Fig. 8**(a) showing the electrochemical test results for the 1st cycle. The current density was increased from 0.07 mA/cm^2 to 0.21 mA/cm^2 (0.1 C) to reactivate the LLZO_V pellet following a slight performance drop experienced during long period storage. After the first activation loop, the test results for the cell operating without an activation procedure between the second and 20th cycles are shown in **Fig. 8**(b).
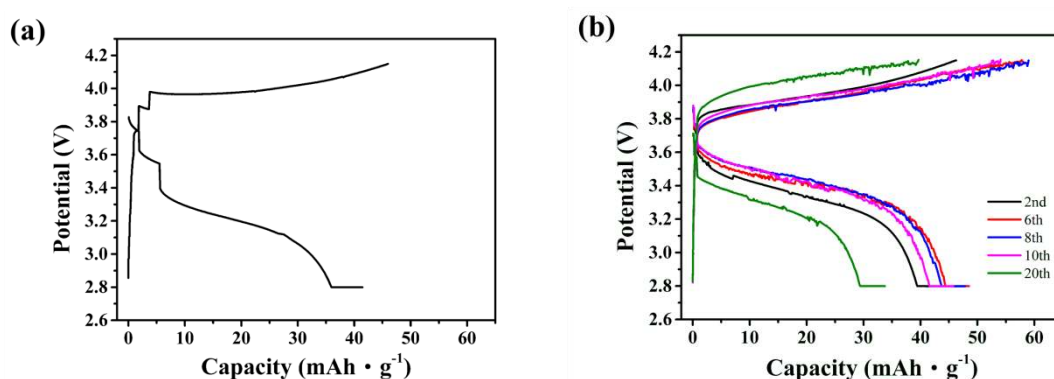
Fig. 8. The (a) 1st and (b) 2nd–20th charge–discharge data for the all solid-state cells.

The capacity slowly increased before the 8th cycle and decreased after that. The polarization between the charge and discharge curves also reached a minimum in the 8th cycle. The curves before the 20th cycle highly resemble that for the standard NCM532 coin cell (**Fig. S3**), with significant polarization occurring. The conductivity of the LLZO pellet increased in the first few cycles, but the cell decayed later on. This phenomenon probably occurred because of the formation of a SEI in the NCM532 slurry. The noisy cycle profile is due to poor interfacial contact and sluggish Li ion transport between Li metal and the surface of LLZO. Although the cell only reached one-third of the theoretical capacity of NCM532, a thinner LLZO pellet, binder

20

that are more compatible with NCM532, and modification of interface such as coating gold or ALD alumina are expected to improve the performance of the all solid-state cells further.[44]

4. Conclusions

The voltammetric treatment of Li | LLZO | Li is found to enhance the conductivity of LLZO while not inducing strong electronic conduction to describe in previous works. Structural and electrochemical characterization of the LLZO before and after voltammetric treatment reveals a Li-ion conduction that increases by a factor of almost 3, whereas the activation energy for the Li-ion diffusion correspondingly decreases from 0.32 eV to 0.26 eV. Neutron powder diffraction and X-ray photoelectron spectroscopy reveal that the combination of increased Li content and the local rearrangement of oxygen induce lower defect oxygen that underpins this conductivity enhancement. An all-solid-state battery using LLZO following voltammetric treatment was demonstrated to be viable. This work has demonstrated a cheap and relatively simple alternative to enhance the conductivity of LLZO compared to other current doping methods. Our approach has given an introductory understanding of conductivity enhancement in all solid state batteries. Further studies like in-situ NPD can be implemented to monitor the real nature of atomic arrangements during cycling of batteries.

ASSOCIATED CONTENT

The supporting information contains refinement parameters for LLZO samples using XRD and NPD data, deconvoluted XPS parameters, photographs of LLZO samples, and coin cell test results. The authors would like to thank the staff members at the Australian Centre for Neutron Scattering, ANSTO for their operations support.

AUTHOR INFORMATION

Corresponding Authors

*Corresponding authors. Tel: +886-2-33661169; Fax: +886 2-23636359

E-mail address: f10381@ntut.edu.tw (HC)

E-mail address: rsliu@ntu.edu.tw (RSL)

Notes

The authors declare no competing financial interests.

REFERENCES

1. Ni, J. E.; Case, E. D.; Sakamoto, J. S.; Rangasamy, E.; Wolfenstine, J. B., Room Temperature Elastic Moduli and Vickers Hardness of Hot-pressed LLZO Cubic Garnet. *J. Mater. Sci.* **2012**, *47*, 7978-7985.

2. Yu, S.; Schmidt, R. D.; Garcia-Mendez, R.; Herbert, E.; Dudney, N. J.; Wolfenstine, J. B.; Sakamoto, J.; Siegel, D. J., Elastic Properties of the Solid Electrolyte $Li_7La_3Zr_2O_{12}$ (LLZO). *Chem. Mater.* **2016**, *28*, 197-206.

3. Song, S.; Yan, B.; Zheng, F.; Duong, H. M.; Lu, L., Crystal structure, Migration Mechanism and Electrochemical Performance of Cr-stabilized Garnet. *Solid State Ionics* **2014**, *268, Part A*, 135-139.

4. Murugan, R.; Thangadurai, V.; Weppner, W., Fast Lithium Ion Conduction in Garnet-Type $Li_7La_3Zr_2O_{12}$. *Angew. Chem. Int. Ed.* **2007**, *46*, 7778-7781.

5. Awaka, J.; Takashima, A.; Kataoka, K.; Kijima, N.; Idemoto, Y.; Akimoto, J., Crystal Structure of Fast Lithium-ion-conducting Cubic $Li_7La_3Zr_2O_{12}$. *Chem. Lett.* **2011**, *40*, 60-62.

6. Awaka, J.; Kijima, N.; Hayakawa, H.; Akimoto, J., Synthesis and Structure Analysis of Tetragonal $Li_7La_3Zr_2O_{12}$ with the Garnet-Related Type Structure. *J. Solid State Chem.* **2009**, *182*, 2046-2052.

7. Rettenwander, D.; Blaha, P.; Laskowski, R.; Schwarz, K.; Bottke, P.; Wilkening, M.; Geiger, C. A.; Amthauer, G., DFT Study of the Role of Al^{3+} in the Fast Ion-Conductor $Li_{7-3x}Al_{3+x}La_3Zr_2O_{12}$ Garnet. *Chem. Mater.* **2014**, *26*, 2617-2623.

8. Buschmann, H., et al., Structure and Dynamics of the Fast Lithium ion Conductor "$Li_7La_3Zr_2O_{12}$". *Phys. Chem. Chem. Phys.* **2011**, *13*, 19378-19392.

9. Bernstein, N.; Johannes, M. D.; Hoang, K., Origin of the Structural Phase Transition in $Li_7La_3Zr_2O_{12}$. *Phys Rev Lett* **2012**, *109*, 205702.

10. Du, F.; Zhao, N.; Li, Y.; Chen, C.; Liu, Z.; Guo, X., All Solid State Lithium Batteries Based on Lamellar Garnet-type Ceramic Electrolytes. *J. Power Sources* **2015**, *300*, 24-28.

11. Bernuy-Lopez, C.; Manalastas, W.; Lopez del Amo, J. M.; Aguadero, A.; Aguesse, F.; Kilner, J. A., Atmosphere Controlled Processing of Ga-Substituted Garnets for High Li-Ion Conductivity Ceramics. *Chem. Mater.* **2014**, *26*, 3610-3617.

12. Li, Y.; Wang, Z.; Li, C.; Cao, Y.; Guo, X., Densification and ionic-conduction improvement of lithium garnet solid electrolytes by flowing oxygen sintering. *J. Power Sources* **2014**, *248*, 642-646.

13. Xu, M.; Park, M. S.; Lee, J. M.; Kim, T. Y.; Park, Y. S.; Ma, E., Mechanisms of Li$^+$ Transport in Garnet-type Cubic $Li_{3+x}La_3M_2O_{12}$ (M = Te, Nb, Zr). *Phys. Rev. B: Condens. Matter* **2012**, *85*, 052301.

14. Miara, L. J.; Ong, S. P.; Mo, Y.; Richards, W. D.; Park, Y.; Lee, J.-M.; Lee, H. S.; Ceder, G., Effect of Rb and Ta Doping on the Ionic Conductivity and Stability of the Garnet $Li_{7+2x-y}(La_{3-x}Rb_x)(Zr_{2-y}Ta_y)O_{12}$ ($0 \leq x \leq 0.375$, $0 \leq y \leq 1$) Superionic Conductor: A First Principles Investigation. *Chem. Mater.* **2013**, *25*, 3048-3055.

15. Düvel, A.; Kuhn, A.; Robben, L.; Wilkening, M.; Heitjans, P., Mechanosynthesis of Solid Electrolytes: Preparation, Characterization, and Li Ion Transport Properties of Garnet-Type Al-Doped $Li_7La_3Zr_2O_{12}$ Crystallizing with Cubic Symmetry. *J. Phys. Chem. C* **2012**, *116*, 15192-15202.

16. Hu, Z.; Liu, H.; Ruan, H.; Hu, R.; Su, Y.; Zhang, L., High Li-ion Conductivity of Al-doped $Li_7La_3Zr_2O_{12}$ Synthesized by Solid-state Reaction. *Ceram. Int.* **2016**, *42*, 12156-12160.

17. Xia, W.; Xu, B.; Duan, H.; Guo, Y.; Kang, H.; Li, H.; Liu, H., Ionic Conductivity and Air Stability of Al-Doped $Li_7La_3Zr_2O_{12}$ Sintered in Alumina and Pt Crucibles. *ACS Appl. Mater. Interfaces* **2016**, *8*, 5335-5342.

18. Cheng, L.; Chen, W.; Kunz, M.; Persson, K.; Tamura, N.; Chen, G.; Doeff, M., Effect of Surface Microstructure on Electrochemical Performance of Garnet Solid Electrolytes. *ACS Appl. Mater. Interfaces* **2015**, *7*, 2073-2081.

19. Sharafi, A.; Meyer, H. M.; Nanda, J.; Wolfenstine, J.; Sakamoto, J., Characterizing the Li–$Li_7La_3Zr_2O_{12}$ Interface Stability and Kinetics as a Function of Temperature and Current Density. *J. Power Sources* **2016**, *302*, 135-139.

20. Suzuki, Y.; Kami, K.; Watanabe, K.; Watanabe, A.; Saito, N.; Ohnishi, T.; Takada, K.; Sudo, R.; Imanishi, N., Transparent Cubic Garnet-type Solid Electrolyte of Al_2O_3-doped $Li_7La_3Zr_2O_{12}$. *Solid State Ionics* **2015**, *278*, 172-176.

21. Tsai, C.-L.; Roddatis, V.; Chandran, C. V.; Ma, Q.; Uhlenbruck, S.; Bram, M.; Heitjans, P.; Guillon, O., $Li_7La_3Zr_2O_{12}$ Interface Modification for Li Dendrite Prevention. *ACS Appl. Mater. Interfaces* **2016**, *8*, 10617-10626.

22. Xu, B.; Duan, H.; Xia, W.; Guo, Y.; Kang, H.; Li, H.; Liu, H., Multistep Sintering to Synthesize Fast Lithium Garnets. *J. Power Sources* **2016**, *302*, 291-297.

23. Cheng, L., et al., Interrelationships Among Grain Size, Surface Composition, Air Stability, and Interfacial Resistance of Al-Substituted $Li_7La_3Zr_2O_{12}$ Solid Electrolytes. *ACS Appl. Mater. Interfaces* **2015**, *7*, 17649-17655.

24. Rajendran, S.; Song, M. S.; Park, M. S.; Kim, J. H.; Lee, J. Y., Lithium Ion Conduction in PVC–$LiN(CF_3SO_2)_2$ Electrolytes Gelled with PVdF. *Mater Lett* **2005**, *59*, 2347-2351.

25. Liss, K.-D.; Hunter, B.; Hagen, M.; Noakes, T.; Kennedy, S., Echidna—The New High-resolution Powder Diffractometer Being Built at OPAL. *Physica B* **2006**, *385–386, Part 2*, 1010-1012.

26. Junji, A.; Akira, T.; Kunimitsu, K.; Norihito, K.; Yasushi, I.; Junji, A., Crystal Structure of Fast Lithium-ion-conducting Cubic $Li_7La_3Zr_2O_{12}$. *Chem. Lett.* **2011**, *40*, 60-62.

27. Zhu, Y.; He, X.; Mo, Y., Origin of Outstanding Stability in the Lithium Solid Electrolyte Materials: Insights from Thermodynamic Analyses Based on First-Principles Calculations. *ACS Appl. Mater. Interfaces* **2015**, *7*, 23685-23693.

28. Sunding, M. F.; Hadidi, K.; Diplas, S.; Løvvik, O. M.; Norby, T. E.; Gunnæs, A. E., XPS Characterisation of in situ Treated Lanthanum Oxide and Hydroxide Using Tailored Charge

Referencing and Peak Fitting Procedures. *J. Electron. Spectrosc. Relat. Phenom.* **2011**, *184*, 399-409.

29. Oldham, K. B., Analytical Expressions for the Reversible Randles-Sevcik Function. *J. Electroanal. Chem. Interfacial Electrochem.* **1979**, *105*, 373-375.

30. Janek, J.; Korte, C., Electrochemical Blackening of Yttria-stabilized Zirconia – Morphological Instability of the Moving Reaction Front. *Solid State Ionics* **1999**, *116*, 181-195.

31. Luer; Janek, J.; Gunther, S.; Kiskinova, M.; Imbihl, R., Microspectroscopy at a Moving Reduction Front in Zirconia Solid Electrolyte. *Phys. Chem. Chem. Phys.* **2002**, *4*, 2673-2679.

32. Kumazaki, S.; Iriyama, Y.; Kim, K.-H.; Murugan, R.; Tanabe, K.; Yamamoto, K.; Hirayama, T.; Ogumi, Z., High Lithium Ion Conductive $Li_7La_3Zr_2O_{12}$ by Inclusion of Both Al and Si. *Electrochem. Commun* **2011**, *13*, 509-512.

33. Kokal, I.; Somer, M.; Notten, P. H. L.; Hintzen, H. T., Sol–gel Synthesis and Lithium Ion Conductivity of $Li_7La_3Zr_2O_{12}$ with Garnet-related Type Structure. *Solid State Ionics* **2011**, *185*, 42-46.

34. Bespalov, I.; Datler, M.; Buhr, S.; Drachsel, W.; Rupprechter, G.; Suchorski, Y., Initial Stages of Oxide Formation on the Zr Surface at Low Oxygen Pressure: An in situ FIM and XPS Study. *Ultramicroscopy* **2015**, *159, Part 2*, 147-151.

35. Valov, I., et al., Electrochemical Activation of Molecular Nitrogen at the Ir/YSZ Interface. *Phys. Chem. Chem. Phys.* **2011**, *13*, 3394-3410.

36. Jung, W.; Tuller, H. L., Investigation of Surface Sr Segregation in Model Thin Film Solid Oxide Fuel Cell Perovskite Electrodes. *Energy Environ. Sci.* **2012**, *5*, 5370-5378.

37. Crumlin, E. J.; Mutoro, E.; Liu, Z.; Grass, M. E.; Biegalski, M. D.; Lee, Y.-L.; Morgan, D.; Christen, H. M.; Bluhm, H.; Shao-Horn, Y., Surface Strontium Enrichment on Highly Active

Perovskites for Oxygen Electrocatalysis in Solid Oxide Fuel Cells. *Energy Environ. Sci.* **2012**, *5*, 6081-6088.

38. Li, J.; Xiong, S.; Liu, Y.; Ju, Z.; Qian, Y., High Electrochemical Performance of Monodisperse $NiCo_2O_4$ Mesoporous Microspheres as an Anode Material for Li-Ion Batteries. *ACS Appl. Mater. Interfaces* **2013**, *5*, 981-988.

39. Li, Y.; Han, J.-T.; Wang, C.-A.; Xie, H.; Goodenough, J. B., Optimizing Li^+ Conductivity in a Garnet Framework. *J Mater Chem* **2012**, *22*, 15357-15361.

40. Labrincha, J. A.; Frade, J. R.; Marques, F. M. B., $La_2Zr_2O_{12}$ Formed at Ceramic Electrode/YSZ Contacts. *J. Mater. Sci.* **1993**, *28*, 3809-3815.

41. Wang, Y.; Richards, W. D.; Ong, S. P.; Miara, L. J.; Kim, J. C.; Mo, Y.; Ceder, G., Design Principles for Solid-state Lithium Superionic Conductors. *Nat Mater* **2015**, *14*, 1026-1031.

42. Agrawal, R. C., dc Polarisation: An Experimental Tool in the Sudy of Ionic Conductors *Indian J. Pure Appl. Phys.* **1999**, *37*, 294-301.

43. Aguesse, F.; Manalastas, W.; Buannic, L.; Lopez del Amo, J. M.; Singh, G.; Llordés, A.; Kilner, J., Investigating the Dendritic Growth During Full Cell Cycling of Garnet Electrolyte in Direct Contact with Li Metal. *ACS Appl. Mater. Interfaces* **2017**, *9*, 3808-3816.

44. Han, X., et al., Negating interfacial impedance in garnet-based solid-state Li metal batteries. *Nat Mater* **2017**, *16*, 572-579.
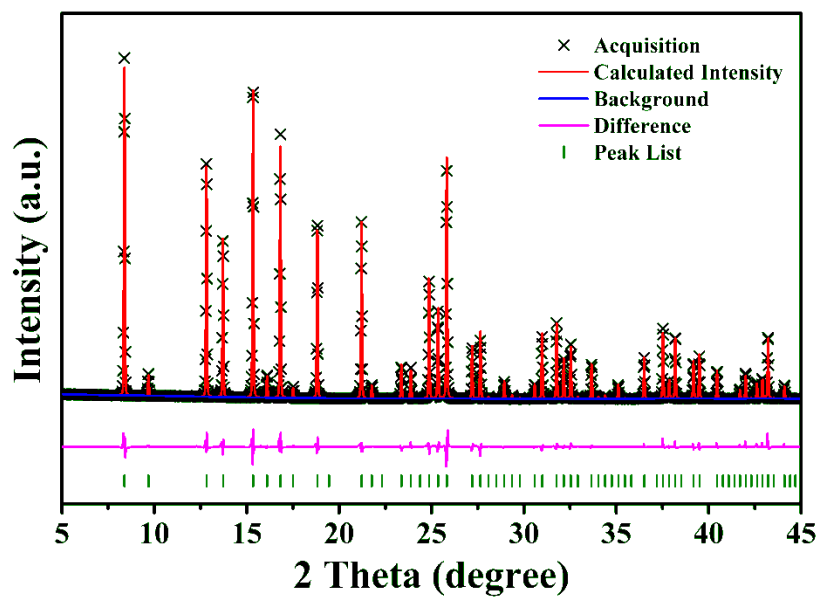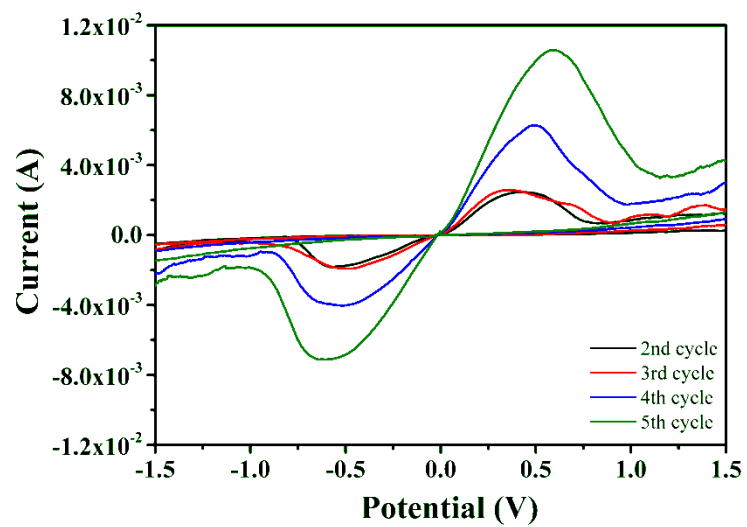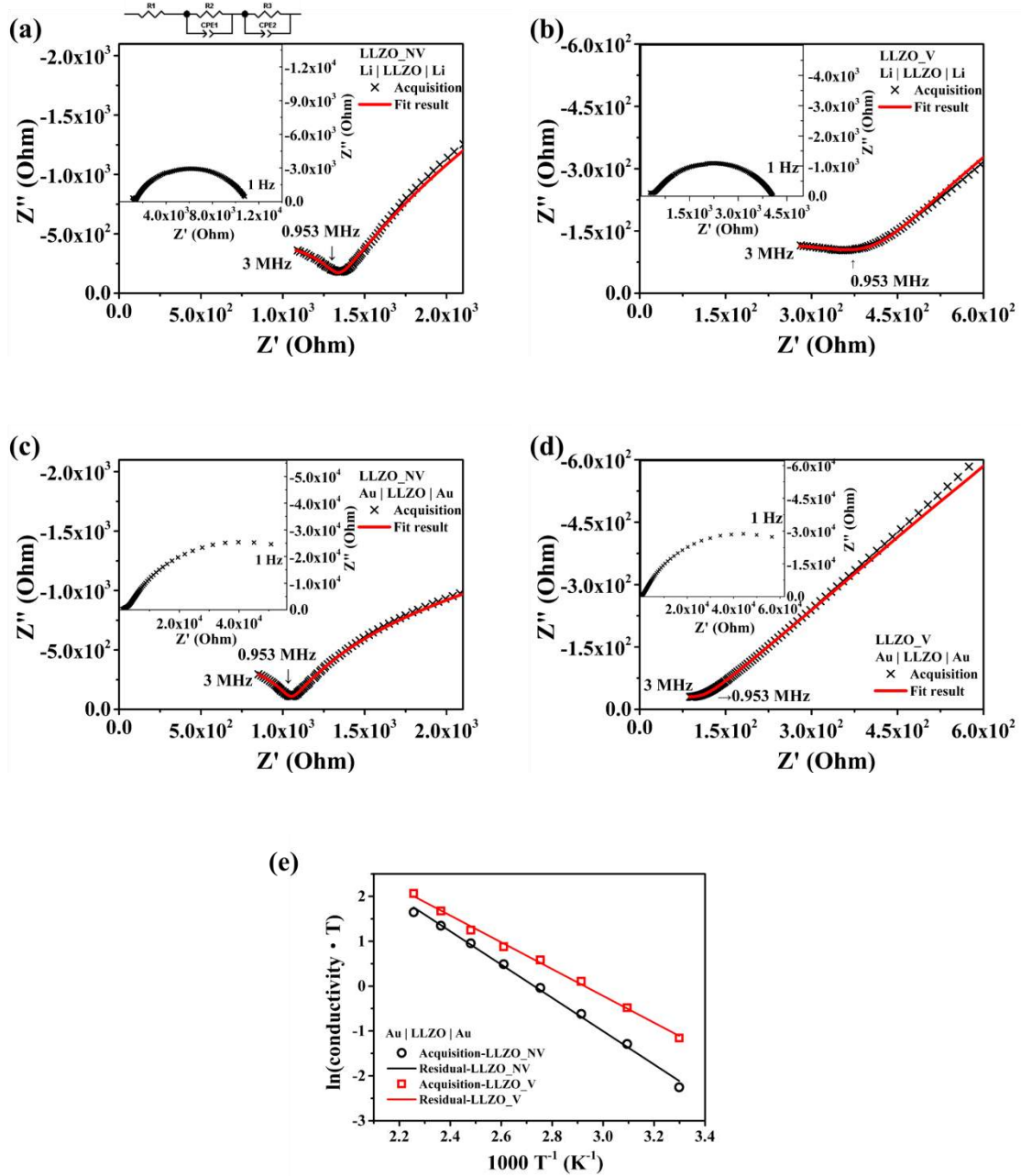
Fig. 1. Rietveld refinement profiles for LLZO using XRD data

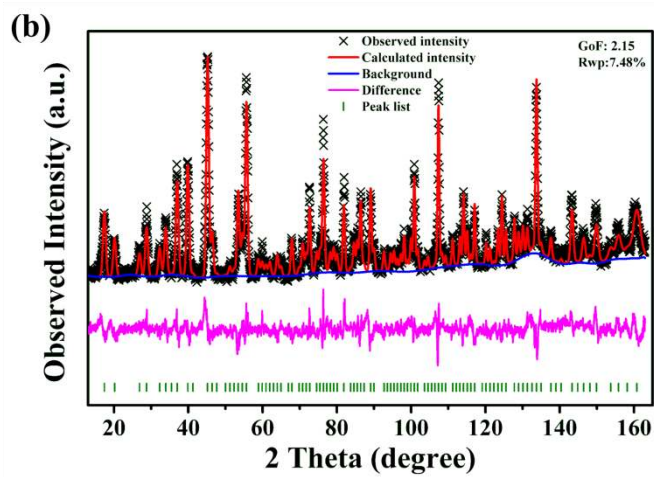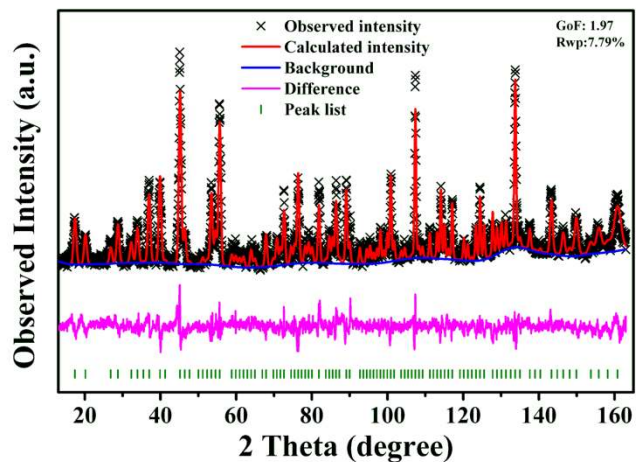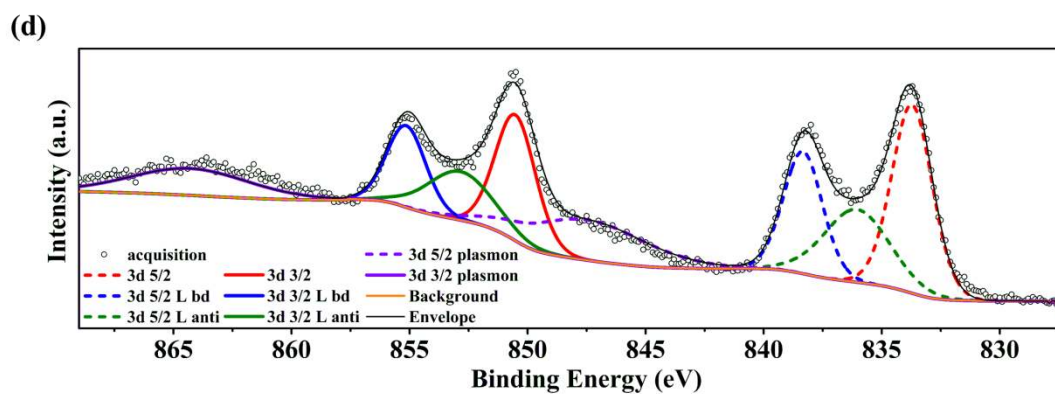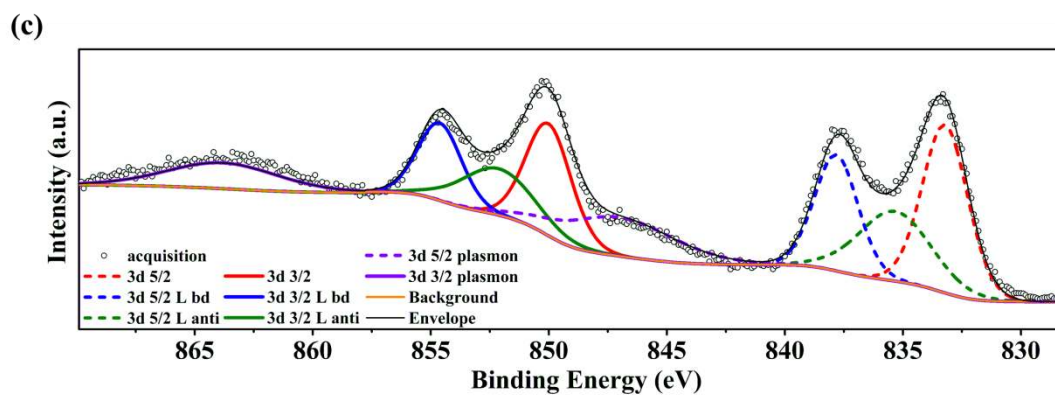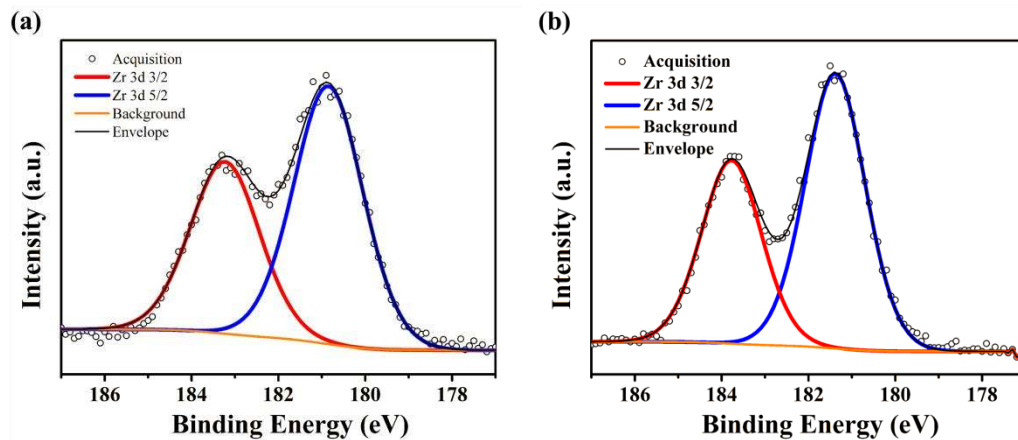**Fig. 2**. The I-V profiles of cyclic voltammetry with Li | LLZO | Li cell.
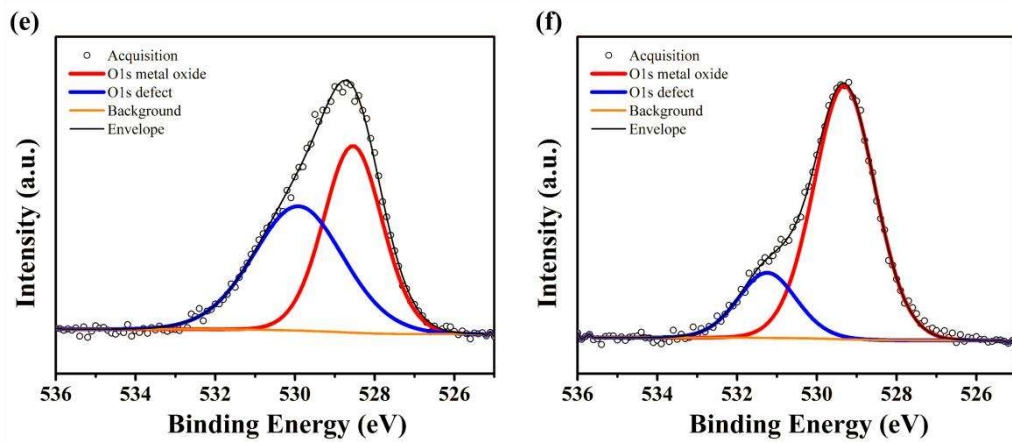
Fig. 3. EIS data and fitting results for LLZO samples in (a), (b) Li | LLZO | Li and (c), (d) Au | LLZO | Au cells. (a), (c) LLZO_NV; (b), (d) LLZO_V; (e) Arrhenius plots of LLZO_NV and LLZO_V.

Fig. 4. Rietveld refinement profiles for LLZO using neutron powder diffraction data (a) before voltammetric treatment and (b) after voltammetric treatment.

Fig. 5. XPS data and deconvoluted Zr 3d spectra for (a) LLZO_NV and (b) LLZO_V, La 3d spectra for (c) LLZO_NV and (d) LLZO_V, and O 1s spectra for (e) LLZO_NV and (f) LLZO_V
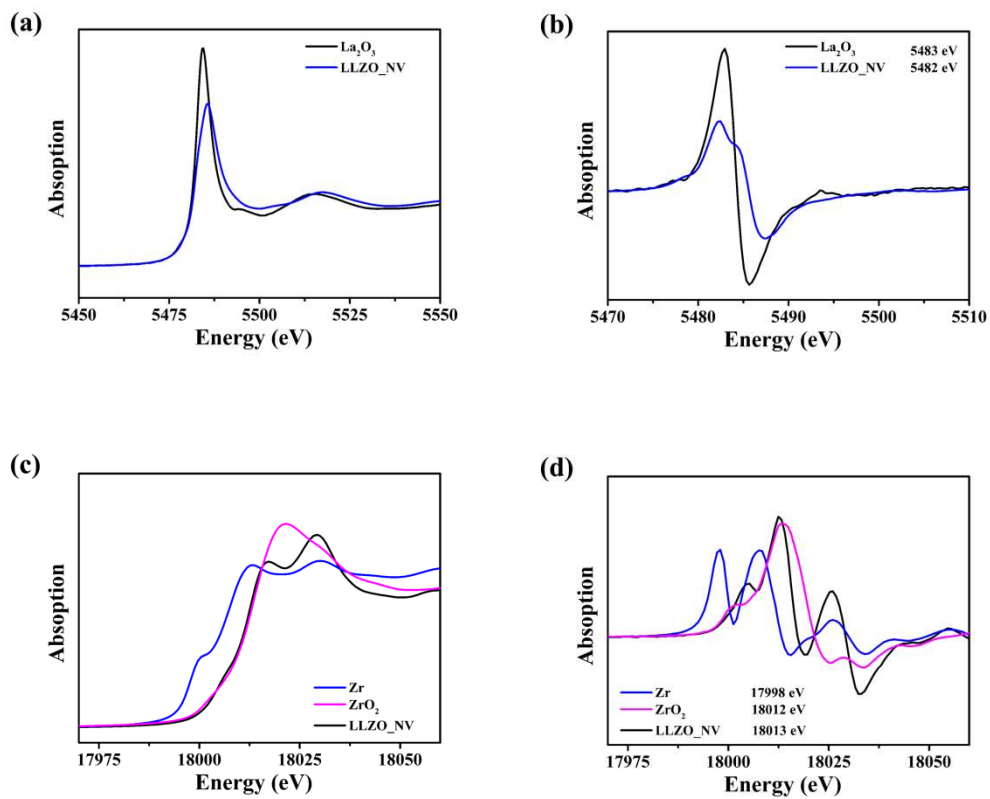
Fig. 6. XANES data at the (a) La L3 and (c) Zr K edge and first derivative of data at the (b) La L3 and (d) Zr K edge
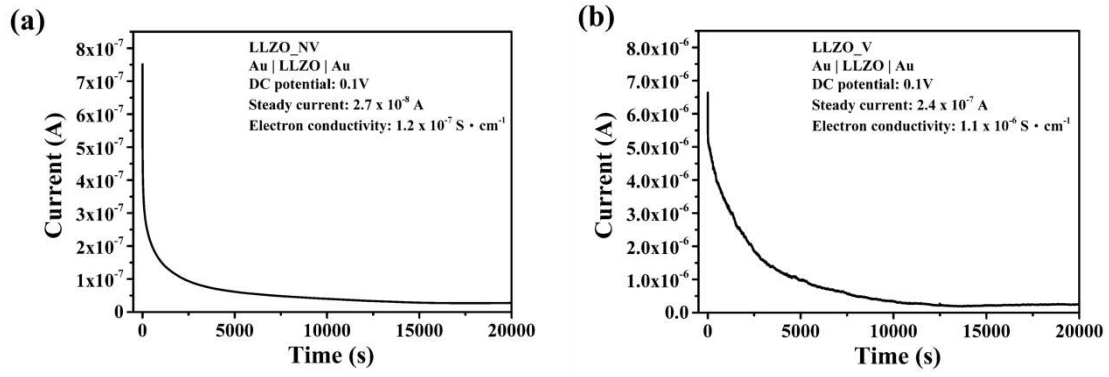
Fig. 7. DC polarization of (a) LLZO_NV and (b) LLZO_V samples.
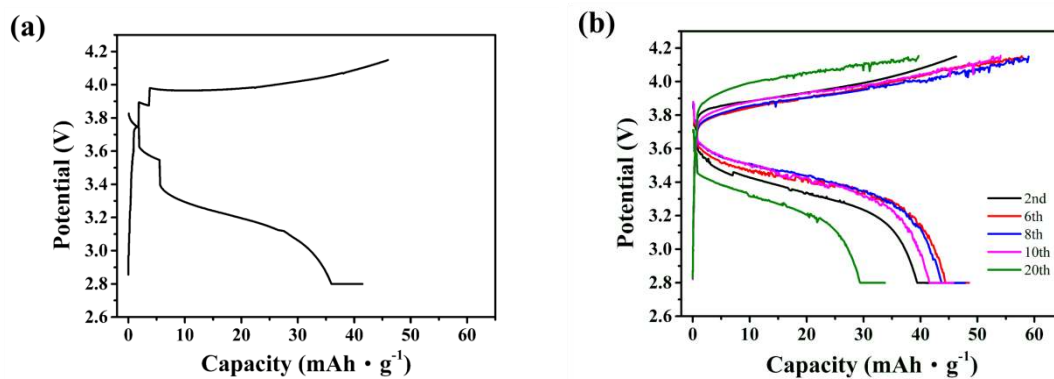
Fig. 8. The (a) 1st and (b) 2nd–20th charge–discharge data for the all solid-state cells.

TOC

Supporting Information

Voltammetric Enhancement of Li-Ion Conduction in Al-doped Li$_{7-x}$La$_3$Zr$_2$O$_{12}$ Solid Electrolyte

Yu-Ting Chen,[†] Anirudha Jena,[†,‡] Wei Kong Pang,[⊥,‖] Vanessa K. Peterson,[⊥,‖] Hwo-Shuenn Sheu,[Δ] Ho Chang,*[‡] Ru-Shi Liu*[†,‡]

† Department of Chemistry, National Taiwan University, Taipei 10617, Taiwan

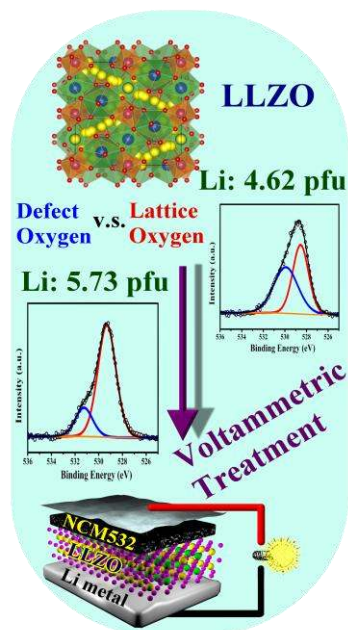‡ Department of Mechanical Engineering and Graduate Institute of Manufacturing Technology, National Taipei University of Technology, Taipei 10608, Taiwan

⊥ Australian Centre for Neutron Scattering, Australian Nuclear Science and Technology Organization, NSW 2232, Australia

‖ Institute for Superconducting and Electronic Materials, University of Wollongong, Squires Way, North Wollongong, NSW 2500, Australia

Δ National Synchrotron Radiation Research Center, Hsinchu 30076, Taiwan

Corresponding authors. Tel: +886-2-33661169; Fax: +886 2-23636359

E-mail address: f10381@ntut.edu.tw (HC)

E-mail address: rsliu@ntu.edu.tw (RSL)

Table S1. XRD Rietveld refinement results for LLZO_NV

	x	y	z	Fraction	U_{iso} (Å^2)
La	0.125	0	0.25	1	0.0108(6)
Zr	0	0	0	1.00(1)	0.00075(7)
O	0.9724(3)	0.0551(6)	0.1487(4)	0.92(2)	0.0107(4)
Li(24d)	0.375	0	0.25	0.22	0.021
Li(96h)	0.094	0.685	0.585	0.36	0.021
Al(24d)	0.375	0	0.25	0.06	0.01

GOF: 1.77   Space group: $I_{a\bar{3}d}$

R_p: 8.24%   Unit Cell Dimension: 12.96278(6) Å

R_{wp}: 10.36%   Volume: 2178.18(1) Å^2

Table S2 (a). NPD Rietveld refinement results for LLZO_NV

	x	y	z	Fraction	U_{iso} ($\mathring{A}^2$)
La	0.125	0	0.25	1	0.004(1)
Zr	0	0	0	1.05(3)	0.005(2)
O	0.9684(3)	0.0544(2)	0.1503(2)	1.00(1)	0.0067(6)
Li(24d)	0.375	0	0.25	0.22(4)	0.021
Li(96h)	0.094(3)	0.686(2)	0.585(2)	0.36(2)	0.021
Al(24d)	0.375	0	0.25	0.06	0.01

GOF: 1.97   Space group: $I_{a\bar{3}d}$

Rp: 5.78%   Unit Cell: 12.9616(4) Å

Rwp: 7.79%   Volume: 2177.57(6) Å^2

Table S2(b). NPD Rietveld refinement results for LLZO_V

	x	y	z	Fraction	U_{iso} (Å^2)
La	0.125	0	0.25	1	0.010(1)
Zr	0	0	0	1.03(3)	0.006(1)
O	0.9686(3)	0.0538(2)	0.1502(2)	1.001(9)	0.0106(6)
Li(24d)	0.375	0	0.25	0.25(4)	0.021
Li(96h)	0.096(2)	0.684(2)	0.583(3)	0.40(2)	0.021
Al(24d)	0.375	0	0.25	0.06	0.01

GOF: 2.15   Space group: $I_{a\bar{3}d}$

Rp: 5.76%   Unit Cell: 12.9620(4) Å

Rwp: 7.48%   Volume: 2177.80(7) Å^2

Table S3 (a). XPS deconvolution results for LLZO_NV.

La	$3d_{5/2}$	$3d_{5/2}$ L bonding	$3d_{5/2}$ L anti-bonding	$3d_{3/2}$
Area	14799	9777	9777	9866
FWHM	2.3	2.2	3.6	2.3
Position	833.2	837.8	835.3	850.0
La	$3d_{3/2}$ bonding	L $3d_{3/2}$ L anti-bonding	$3d_{5/2}$ plasmon	$3d_{3/2}$ plasmon
Area	6518	6518	8316	5543
FWHM	2.2	3.6	5.5	5.5
Position	854.6	852.1	847.0	863.8
Zr		$3d_{5/2}$		$3d_{3/2}$
Area		7574		5049
FWHM		1.9		1.9
Position		180.8		183.2
O		**1s oxide lattice**		**1s defected**
Area		7284		7442
FWHM		1.7		2.7
Position		528.5		529.9

Table S3 (b). XPS deconvolution results for LLZO_V.

La	$3d_{5/2}$	$3d_{5/2}$ L bd	$3d_{5/2}$ L anti	$3d_{3/2}$
Area	16279	10139	10139	10853
FWHM	2.0	1.9	3.3	2.0
Position	833.7	838.3	836.1	850.5
La	$3d_{3/2}$ L bonding	$3d_{3/2}$ L anti-bonding	$3d_{5/2}$ plasmon	$3d_{3/2}$ plasmon
Area	6759	6759	10100	6734
FWHM	1.9	3.3	5.9	5.9
Position	855.1	852.9	847.5	864.3
Zr	$3d_{5/2}$			$3d_{3/2}$
Area	7708			5319
FWHM	1.6			1.6
Position	181.4			183.8

O	1s oxide	1s defect
Area	11783	2879
FWHM	1.80573	1.71506
Position	529.3	531.2

Figure S1. (a) LLZO_NV pellets (left) and LLZO_V pellets (right). (b) Cross-section of LLZO_V pellet.

(a)   (b)
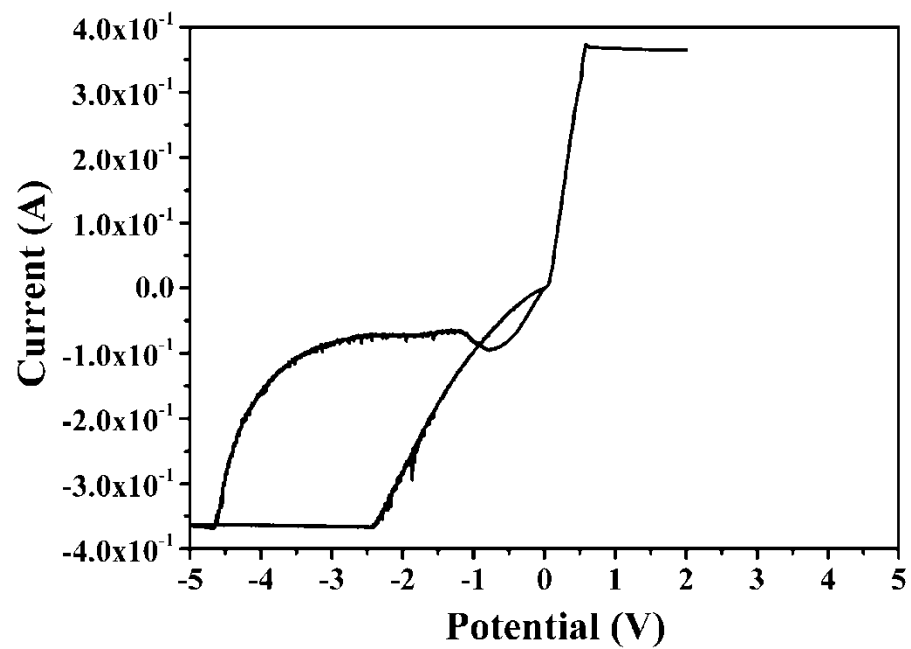
Figure S2. (a) Photograph of pellets after 5th and 8th cycles (b) The 8th cycle I-V profile of an over-treated LLZO pellet

(a)

(b)

Figure S3. Charge–discharge test results for of the NMC coin cell

1st cycle of NCM523
Coulombic efficiency = 87.8 %

147.0 mAh g^{-1}

129.1 mAh g^{-1}